



Magnetorheological behavior of thermoplastic elastomeric honeycomb structures fabricated by additive manufacturing

Somashree Mondal^{a,b,*}, Robert Katzschmann^b, Frank Clemens^{a,**}

^a Department of Functional Materials, Empa – Swiss Federal Laboratories for Materials Science and Technology, Dübendorf, Switzerland

^b Soft Robotics Laboratory, ETH – Swiss Federal Institute of Technology, Zürich, Switzerland

ARTICLE INFO

Handling Editor: Dr Uday Vaidya

Keywords:

Magnetorheological elastomer
Soft magnetoactive composites
Material extrusion
Additive manufacturing
Magnetorheological effect
Honeycomb structure

ABSTRACT

3D printing of magnetorheological elastomers (MREs) can potentially create versatile and complex mechanical structures with reversible stiffening properties. Several additive manufacturing (AM) methods, like direct printing and stereolithography (SLA), have been used to achieve magnetic thermoset and elastomer composite structures. For the first time, we demonstrate the use of MREs based on thermoplastic elastomers (TPE) in AM and we investigate their magnetorheological (MR) effect when used in lightweight honeycomb designs. Due to the low shore hardness of TPE, a screw extruder-based printing head is employed to print disk-shaped samples with honeycomb patterns at infill percentages varying from 15% to 50%. In order to compare the MR effect of disks with varying honeycomb infills through a compression method, we investigated the effect of different testing configurations. We observe that different permanent magnet configurations, as it has been used in literature so far, create an additional effect on the measured MR effect of the MRE samples. To eradicate this effect, a test setup with an unpaired permanent magnet configuration is proposed. MRE structures with an infill density of 20% showed, at 1% deformation range, the highest MR effect, almost four times as high as 100% infilled samples. MRE structures with an infill density between 30% and 50% showed a lower MR effect than at 20%, but were still higher than at 100%. We observe in simulations that the magnetic flux density of 100% infilled samples was higher at the edges of the samples and lower at the center. For samples with honeycomb infill, the magnetic flux density was higher at the outer rim of the samples and edges of the walls within the sample, which causes a higher MR effect. Our work demonstrates that the MR effect can be tuned by designing a MRE structure with a honeycomb infill. The honeycomb infill results in lightweight MREs with improved MR effect useful for various downstream applications that require reversible strong stiffening while remaining comparatively lightweight.

1. Introduction

Magnetorheological elastomers can be categorized as “smart” or “intelligent” materials by virtue of their reversible stiffening properties under the application of an external magnetic field [1,2]. The reversible change in stiffness of the MRE is called the magnetorheological (MR) effect [3]. MREs primarily comprise a polymeric matrix and nano/micro-sized magnetic filler particles. The filler particles can be distributed in the polymer matrix in an aligned manner, called anisotropic MRE, or can be distributed randomly, termed isotropic MRE [2,4,5].

Fabrication of MREs is usually done using conventional molding and

casting techniques [6]. Various polymer matrix materials like natural rubber [7–9], silicone [10–12], polyurethane [13,14], and thermoplastic elastomers [2,15] are employed in the process. The fabrication process involves mixing an elastomer matrix material with magnetic particles, casting the mixed composite into a desired shape, and curing the composite with or without the application of an external magnetic field. Recently, additive manufacturing has paved the way for the innovative fabrication of smart composite materials. Several works have been reported that involve the 3D printing of magnetic composite materials and their wide range of applications, namely mechanical reinforcements [16,17], electronic components [18], and magnetic robots [19–22].

AM techniques like direct ink writing and stereolithography (SLA)

* Corresponding author. Department of Functional Materials, Empa – Swiss Federal Laboratories for Materials Science and Technology, Dübendorf, Switzerland.

** Corresponding author.

E-mail addresses: somashree.mondal@empa.ch (S. Mondal), frank.clemens@empa.ch (F. Clemens).

Nomenclature

3D	Three-dimensional
MREs	Magnetorheological elastomers
AM	Additive manufacturing
SLA	Stereolithography
MR	Magnetorheological
TPE	Thermoplastic elastomers
FDM	Fused Deposition Modelling
UV	Ultra Violet
ABS	Acrylonitrile Butadiene Styrene
PLA	Polylactic Acid
MEX	Material Extrusion
FFF	Fused Filament Fabrication
SEBS	Styrene-Ethylene-Butylene-Styrene
CIP	Carbonyl Iron Powder
μm	micrometer
vol%	Volume percentage
rpm	Rotation per minute
kV	Kilo Volt
T	Tesla

have been investigated for developing magnetic composite structures. Bastola et al. used direct ink writing for the development of MRE structures by encapsulating MR fluid and MR elastomer in a silicone matrix [23–25]. A similar approach was reported earlier by Krueger et al., where they dispensed magnetic powder in a silicone matrix [26]. However, direct ink writing has some disadvantages in comparison to the fused deposition modeling (FDM) process, like its comparatively low resolution and slow printing speed.

Ji et al. [27] and Lantean et al. [28] developed soft magneto-responsive materials using the SLA method. A photocurable resin with dispersed magnetic nanoparticles was formulated and printed into soft-magnetic structures. Although SLA can be used to develop structures with high precision, there are limitations in the range of useable resins, magnetic filler content, and the need for post-processing; the SLA-printed structures often need cleaning and additional UV curing after print completion. Higher filler content can hinder the efficiency of UV curing due to reduced light penetration and light scattering.

The FDM method has an added advantage when compared to direct ink writing or SLA. Using FDM-based 3D printing, a wide range of polymers can be printed into complex shapes with higher time efficiency. The fused deposition modeling, which is recently, also termed the material extrusion-based additive manufacturing method [29], has already been used for developing soft magnetic polymer composites by Khatri et al. [30]. Their work demonstrated that by increasing the filler content of steel powder inside an ABS polymer matrix, the magnetic flux density in the 3D printed structure increased. Ralchev et al. [31] investigated the magnetic properties of FDM printed magnetic structures with different design variations. The work reportedly used polylactic acid (PLA) and iron microparticle composite filaments for the printing process with different infill patterns. Their work also highlighted that the relative magnetic flux density decrease with lowering the density of the infill patterns through the 3D printing process. It is worthwhile to mention that even though PLA and ABS are thermoplastic matrix materials, they are not suitable for magnetorheological applications owing to their rigidity and lack of elastomeric properties.

Lightweight cellular structures are potential candidates for various engineering applications. Of the various types, honeycomb structures have been widely reported in the literature and have demonstrated better performance than solid structures [32,33]. Their mechanical properties can be tuned by adjusting geometric parameters like honeycomb cell size, angles between walls, thickness, etc. [34,35].

Honeycomb structures can be used in sandwich structures as core materials, and as shock absorbers owing to their high energy adsorption capacity [32,35,36]. Fabrication of such honeycomb structures has been made feasible with the advances in 3D printing technology. Li et al., combined numerical methods, experiments, and 3D printing to develop a programmed sandwich structure containing 3D printed honeycomb cores [36]. Chen et al., employed a 3D printing technique to develop a new class of hierarchical honeycomb and investigate their mechanical properties at a large compressive deformation range [37]. Although honeycomb structures are being actively fabricated with different metals, polymeric resins, or thermoplastic for various mechanical properties, these structures have not yet been investigated as magnetorheological materials.

Magnetorheological behavior of MREs has been explored using magneto-mechanical analysis methods like shear deformation [38–40], uniaxial compression [40–42], and tensile testing [40,43]. The characterization methods involve the use of an external magnetic field to measure the magnetorheological effect in the elastomer-based composite. Schubert and Harrison compared three different magneto-mechanical analysis methods, namely uniaxial compression, uniaxial tension, and pure shear deformation, to investigate the MR effect of their silicone-carbonyl iron composites [40]. Depending on the test method they used, the MR properties differed significantly. Both Gordaninejad et al. and Li et al. reported a higher MR effect in compression testing compared to the shear mode testing [18,19]. This observation is owed to the fact that in compression loading mode the distance between the magnetic particles decreases. Furthermore, studies on effect of various test parameters on magnetorheological properties of MREs in compression mode has also been performed. It has been reported that pre-strain has a strong influence on the MR effect in compression mode and with increasing pre-strain, a decrease in relative MR effect has been observed [44]. Vatandoost et al., investigated the effect of shape factor on the MR effect and concluded that an increase in shape factor also leads to increment of MR effect in cylindrical shaped MREs [45]. Studies have also shown that particle volume fraction has an effect on the magnetorheological properties under compression mode [46,47]. To investigate the magneto-mechanical behavior by a compression method, an external magnetic field has been applied by permanent magnets [48–50] and electromagnets [41,42]. Typically the setup for electromagnets is bulky and researchers have optimized the electromagnet shape to build a compact yet efficient test setup [48].

One of the major drawbacks of electromagnets is the heating of the sample during the testing process which can be avoided by using massive iron cores to increase the heat capacity, however, that leads to a bulky test setup. Therefore, for material development, researchers have started to use paired and unpaired permanent magnet configurations. Koo et al. [48] and Wan et al. [49] placed permanent magnets on the top and the bottom of the samples (also termed paired permanent magnet configuration) for their compression tests. In contrast, Mistik et al. used an unpaired magnet configuration by placing permanent magnets below the sample during the compression test [51]. A key point that one has to consider is that in compression mode with paired magnet configuration, the magnetic forces and the mechanical forces act in parallel directions, thereby resulting in a pre-compression which further leads to an over-estimated MR effect of the composite [5,44].

For the first time, we investigate a honeycomb-based lightweight structure concept in MREs using the thermoplastic material extrusion (MEX) based AM process [29], well known as FDM or fused filament fabrication (FFF). We aim to investigate the MR effect of MRE honeycomb-patterned structures by varying the infill density parameter during the printing process. Due to the low Shore hardness (Shore 30A) of the MRE, a filament printing head is not suitable, thereby, a screw-extruder-based printing head, also termed pellet extruder, is used for the 3D printing of MRE honeycomb structures. With the aid of pellet extrusion-based FDM printing, it is possible to print materials with shore hardness comparable to that of silicone. Prior to the analysis of the

magneto-mechanical properties, we performed an evaluation and investigated some setup parameters that affect the MR effect of the composite structures.

2. Materials and methods

2.1. Raw materials

A styrene-ethylene-butylene-styrene block copolymer (SEBS), KTF ATL 2, with Shore A hardness 22, and density of 1.02 g/cm^3 (Kraiburg TPE, Waldkraiburg, Germany) was used as the matrix material. CC-grade carbonyl iron powder (BASF, Ludwigsburg, Germany) was used as the soft ferromagnetic filler material. The carbonyl iron powder (CIP) is coated with SiO_2 layer and has an average size (d_{50}) and density of $4.7 \mu\text{m}$ and 7.89 g/cm^3 , respectively. To investigate the magneto-mechanical compression setup, other SEBS materials (Kraiburg TPE, Waldkraiburg, Germany) with a Shore A hardness of 30, 48 and 70, were used.

After printing the different honeycomb samples, the cavity cells of the honeycombs were infiltrated with silicone Ecoflex 00–10 (Smooth-on, Inc., Macungie, Pennsylvania, USA) by casting process. The infiltration maintained the honeycomb structure during testing. The Shore A hardness of the liquid silicone Ecoflex 00–10 after curing was measured to be Shore 8A.

2.2. Compounding and pellet fabrication

A torque rheometer, HAAKE PolyLab Rheomix 600 from Thermo-fisher (Karlsruhe, Germany), was used for the compounding process. The SEBS was heated to 180°C in the high shear mixer and 30 vol.-% of CIP was added to the polymer in short intervals. The compounding was performed at 30 rpm for 30 min. The resulting composite was then extruded into 1.75 mm filaments using a capillary rheometer RH7 from NETZSCH (Selb, Germany) at 180°C and at a speed of 10 mm/min. A constant pressure of 20 bar was measured during the extrusion process. After extrusion, the filaments were manually pelletized with a scissor. A pellet extrusion-based 3D printer, Voladora NX+ from International Technology 3D Printers, S.L. (Valencia, Spain), was used to produce samples with different infill densities. A schematic of the MRE fabrication process is highlighted in Fig. 1.

2.3. Pellet-extrusion based 3D printing

A simple cylindrical design was used to generate various samples with interior honeycomb structures with varying infill percentages as shown in Table 1. Given a honeycomb pattern, the infill percentages varied between 15% and 50% by adjusting the infill percentage parameter in the slicer software Simplify3D. The slicer software generated G-codes that were loaded in the web browser control of the Voladora NX+ 3D printer. The temperature of the extruder and the print bed was set to 220°C and 50°C , respectively. For all printed structures, nozzle diameter of 0.8 mm and an extrusion multiplier of 16 were

Table 1

Sample naming convention.

Magnetic filler content (vol.-%)	Honeycomb infill density%	Sample name
0	100	SEBS
30	15	SEBS-30CIP-15
30	20	SEBS-30CIP-20
30	25	SEBS-30CIP-25
30	30	SEBS-30CIP-30
30	40	SEBS-30CIP-40
30	50	SEBS-30CIP-50
30	100	SEBS-30CIP-100

selected. A printing speed of 15 mm/s was used for all the different samples. In addition to the honeycomb structures, samples with 100% infill were printed with 0% and 30% CIP filler content to investigate the right compression setup for the study (see Section 2.4.3). The naming convention of samples is mentioned in Table 1. All the mentioned MRE samples were printed with a diameter of 25 mm and a height of 5 mm. Additionally, SEBS-30CIP-100 samples were also printed with heights of 3 and 7 mm. After printing, all honeycomb structures were infiltrated with Ecoflex 00–10 (Shore hardness 8A), as shown in Fig. 2b. An image of SEBS-30CIP-100 is shown in Fig. S1. The structural stiffness of the honeycomb samples made by 15% infill density was too low and therefore deformation in its structure could be observed by applying an external magnetic field.

2.4. Characterization technique

2.4.1. Scanning electron microscopy

To investigate the morphology of the carbonyl iron powder, scanning electron microscope (SEM) experiments were performed using Tescan Vega 3, TESCAN, Brno (Kohoutovice, Czech- Republic). High vacuum mode and 10 kV accelerating voltages were needed to achieve high-resolution images. The powder was plated with a thin layer of carbon before image analysis.

In order to observe the distribution of the CIP particles in the TPE matrix, a cross-section view and a side view of a 3D printed SEBS-30CIP sample were observed using Quanta 650 Environmental Scanning Electron Microscope (ESEM) from FEI, (Oregon, United States). An accelerating voltage of 20 kV was used to obtain the images.

2.4.2. Vibrating sample magnetometer

The magnetization of the MRE composite with 30 vol.-% CIP was measured using a vibrating sample magnetometer (VSM) from Quantum Design (San Diego, USA). A 0.095 g SEBS-30CIP sample and an out-of-plane sample holder were used for the VSM measurements. A magnetic field from 0 T to 2.5 T at $\sim 0.1 \text{ T/min}$ was applied and the temperature was kept constant at 300 K.

The $M-H$ curve derived from the data is further plotted in Fig. S5 and the magnetic permeability of the composite was calculated.

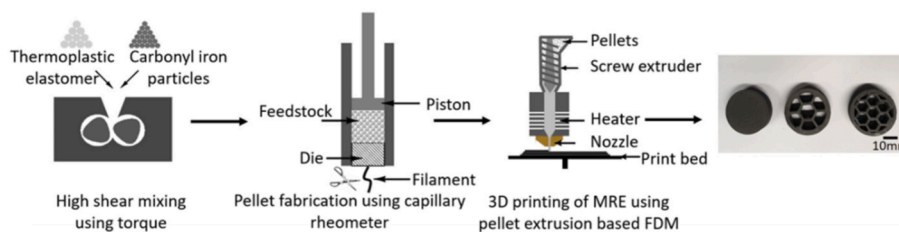


Fig. 1. Fabrication process of MRE samples. Thermoplastic elastomer (TPE) and carbonyl iron powder were mixed above the melting temperature of the TPE. The MRE was extruded into a filament that was later cut into pellets suitable for feeding into the printer head with screw extruder. The MRE samples were printed with different infill densities.

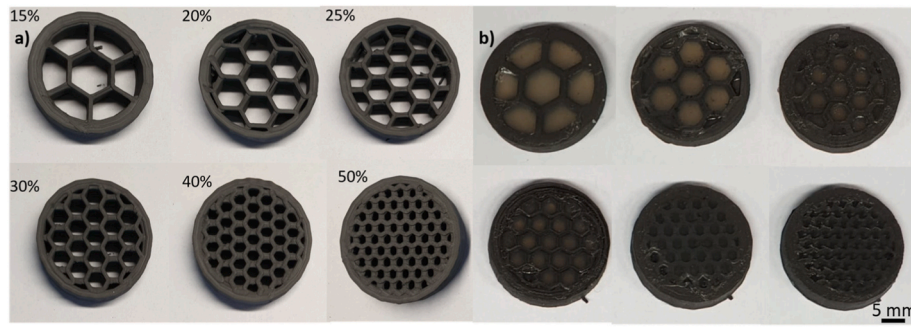


Fig. 2. SEBS-30CIP samples printed with different infill density percentages from 15% to 50%. All samples were printed with a diameter of 25 mm and a height of 5 mm. a) Samples as printed b) Samples infiltrated with silicone (Shore hardness 8A after curing).

2.4.3. Magneto-mechanical characterization

A universal testing machine Z005 from Zwick Roell GmbH & Co. (Ulm, Germany) was used for the magneto-mechanical analysis of the samples in compression mode. The setup consisted of the 5 kN load cell, a probe, aluminum sheets for magnetic shielding, and permanent NdFeB magnets (Webcraft GmbH, Uster, Switzerland). N45 NdFeB disc-shaped permanent magnets with a diameter of 30 mm and a height of 3 mm with the remanent magnetization of 1.32–1.37 T and relative magnetic permeability (μ_r) of 1.05 were used to study the compression setup. To investigate the magneto-mechanical compression setup, the external magnetic field was varied by stacking permanent NdFeB magnets with a thickness of 3 mm on top of each other. The magnetic flux, achieved by the number of stacked magnets, was measured by a magnetic field meter (AC/DC Magnetic Meter, Extech Instruments, Nashua, USA) and simulated using FEM analysis (FEMM, an open-source platform built by David Meeker). For the magneto-mechanical analysis of the honeycomb samples, a single NdFeB hard ferromagnet with 10 mm height and 30 mm diameter was used. The 3 mm NdFeB magnets were used in both paired and unpaired configurations. For the paired magnet configuration, a different number of permanent magnets were placed on the top and the bottom of the MRE samples. For the unpaired magnet configuration, the magnets were placed on the bottom of the sample. An image of the two setups used for this study is demonstrated in Fig. 3.

To investigate the effect of the test parameters, like magnet configuration, pre-load, sample height, and material stiffness, preliminary compression tests were performed with both the paired and unpaired magnet configuration using samples SEBS and SEBS-30CIP-100. Stacks of 3 mm thick NdFeB magnets and a 10 mm thick NdFeB single ferromagnet (large magnet) were used to vary the magnetic field.

A pre-loading force is commonly used in compression tests to ensure sufficient contact between the disc-shaped sample and the probe of the testing machine. Additionally, a pre-loading force also takes into account the scenario where the MRE can be prone to experiencing a static strain during its use in an application. Unfortunately, a pre-load on considerably soft material results in a pre-compression which further has a considerable effect on the MR effect [44]. For the compression testing of MREs, different pre-compression values have been reported [48,52]; however, the required pre-loads to achieve these pre-compression values have not been reported. Brancati et al. used a high pre-load variation between 200 N and 700 N to investigate the influence of axial pre-load on the stiffening effect of the MRE. In contrast to these high pre-load values, Li et al. used a constant pre-load of 15 N for their compression tests [53,54].

To investigate the effect of the pre-load on the magneto-mechanical compression setup, plain SEBS samples were investigated. In this study, the term compression has been used from hereon to define the contraction of the height that the sample undergoes during the compression tests. For both paired and unpaired magnet configurations, a constant compression of 1% was applied after applying a pre-load of 1 N and 10 N, respectively.

The calculation of the MR effect is done by using the compression modulus of the MRE with and without an external magnetic field, derived from the compression tests. The MR effect is calculated by the following formulae,

$$\text{Relative MR effect [\%]} = \frac{E_s - E_0}{E_0} \cdot 100 \quad (1)$$

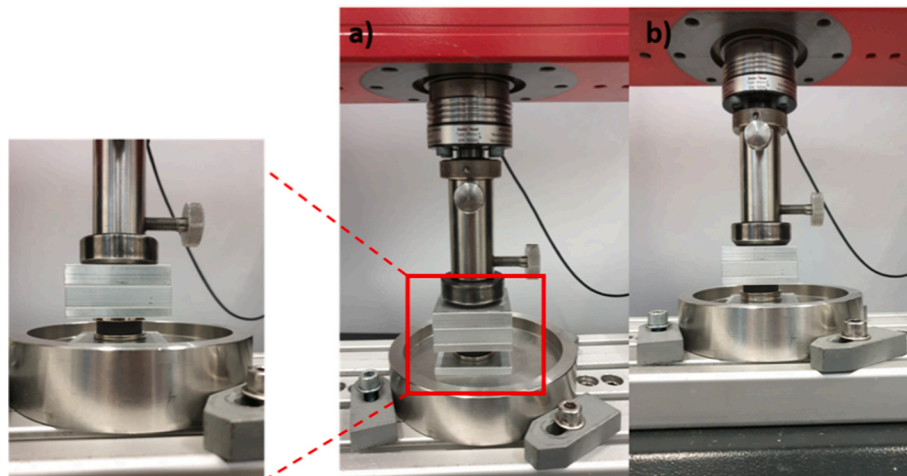


Fig. 3. Two magneto-mechanical compression setups to investigate the MR effect of 3D printed samples. a) paired magnet configuration with one pair of magnets and sample in between; b) unpaired magnet configuration with two unpaired magnets underneath the sample.

$$\text{Absolute MR effect} = E_s - E_0 \quad (2)$$

where E_s is the slope of the stress-strain curve of the MRE under a magnetic field and E_0 is the slope of the stress-strain curve in absence of an external magnetic field. At the beginning of this study, the magneto-mechanical compression test setup was investigated with a pure SEBS sample, as mentioned above, and therefore stiffening effect in these samples was also analyzed using Equation (1). For compression testing, a pre-loading force is commonly used to ensure contact between the test specimen and the testing probe of the machine. In this study, a preload of 1 N, a pre-compression of 10% and a further compression of 1%, 2%, 4% and 10% were used for the different cyclic magneto-mechanical measurements.

3. Results and discussion

3.1. Microstructure analysis and magnetization behavior of CIPs and MRE composites

To investigate the morphology of the CIP particles, SEM analysis was performed. As shown in Fig. S2, the particle size of $2 \pm 0.75 \mu\text{m}$ of the spherical carbonyl iron particles was calculated using ImageJ (National Institutes of Health, Maryland, USA). The analyzed particle size was slightly smaller in comparison to the datasheet information obtained by BASF ($4.7 \mu\text{m}$). As seen in Fig. S2, agglomerates of spherical particles with smaller particles attached to the surface can explain the difference between the image analysis and the data sheet given by the supplier. Furthermore, we can see the nature of CIP particle distribution in the thermoplastic elastomeric matrix after printing in Fig. S3. As shown in the SEM analysis, the particle distribution is homogeneous within the thermoplastic matrix. Additionally, to confirm the homogeneous distribution of the CIP particles a capillary rheometry analysis was done. As depicted in Fig. S4 a constant pressure was achieved during the extrusion process.

Magnetization of the MRE composite with 30 vol.-% CIP was investigated by VSM and a saturation magnetization of 0.65 T was analyzed. Using the mixing rule equation:

$$B_{(\text{composite})} = B_{(\text{CIP})} \bullet 0.3 + B_{(\text{SEBS})} \bullet 0.7 \quad (3)$$

where $B_{(\text{composite})}$ is the saturation magnetization of the composite and the value for pure carbonyl iron can be calculated. Since SEBS is a paramagnetic material, the respective term can be neglected and a value of 2.17 T for pure carbonyl iron is calculated. The calculated value is similar to the theoretical value of iron (2.2 T).

In order to calculate the magnetic permeability, the $M - H$ curve is plotted as demonstrated in Fig. S5. Magnetic permeability (μ) can be derived from the slope of the $M - H$ curve using the following equation,

$$\mu = \frac{dM}{dH} + 1 \quad (4)$$

It is noteworthy, that Equation (4) holds only when both M and H are represented in the same unit, as in this case kA/m.

3.2. Experimental analysis and simulation of permanent magnet configuration

The resulting magnetic flux from the paired and unpaired magnet configuration is presented in Fig. 4, and it is evident that paired magnets result in higher magnetic flux. However, for a low number of magnets, the magnetic flux for both configurations is observed to be similar. The measurements for paired configuration were done by placing the magnetic field meter probe in between the stacked pair of magnets while for the unpaired magnet configuration, the probe was placed on top of the stack of magnets. For all experimental analyses, a deviation of $\pm 10 \text{ mT}$ was observed.

Fig. 4 shows that the simulated magnetic flux is lower in comparison to the magnetic flux derived from experimental data. The discrepancy is because a theoretically correct relative magnetic permeability (μ/μ_0) of 1.05 for the N45 permanent magnet was used in the simulation. The value for the N45 magnets used for the measurements seems to be higher in reality.

3.3. Effect of compression test setup on magnetorheological behavior

The results of compression tests with 1 N and 10 N are plotted against the force-compression curve of the sample measured with 0.1 N pre-load (Fig. S6). A pre-load of 1 N and 10 N results in a pre-compression of 6% and 10%, respectively. It is evident that a higher pre-load resulted in a higher deformation, however, for hyperelastic materials this results in a slope change (i.e., compression modulus change). Brancati et al. demonstrated in their work, that a large pre-load leads to a higher slope of the force-deformation curve with and without an applied magnetic field [53].

As shown in Fig. S6, the pre-compression shifts to higher values when applying an external magnetic field. The increase in pre-compression value is significantly higher when using a paired magnet configuration in comparison to an unpaired magnet configuration. The pre-compression can be calculated by the following equation:

$$\epsilon_{\text{pre-compression}} = \epsilon_{\text{pre-load}} + \epsilon_{\text{magnetic field}} \quad (5)$$

It is worthwhile to mention that when a pre-load of 10 N was applied to the MRE samples, the change of the slope was significantly smaller in comparison to 1 N pre-load (see Fig. S6). For the setup of two paired magnets, the pre-compression was two and three times higher than the pre-compression without magnetic field (for 1 N and 10 N pre-load, respectively). Using four unpaired magnets, the pre-compression only increased by 33% and 20% for 1 N and 10 N pre-load, respectively.

In Fig. 5, the MR effect in SEBS-30CIP-100 samples and the stiffening

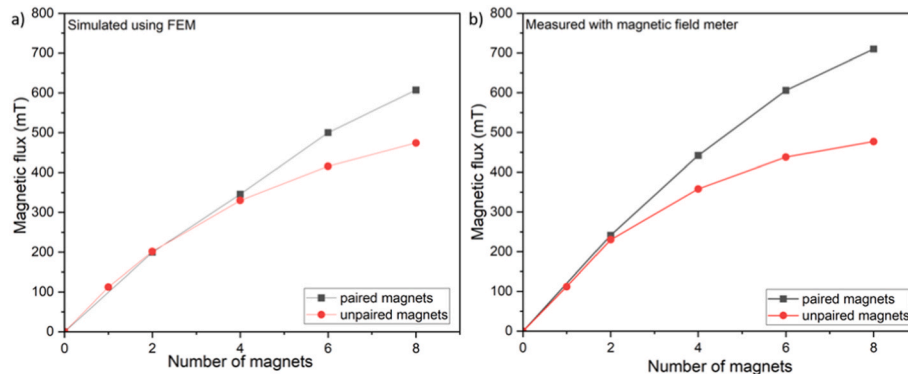


Fig. 4. Magnetic flux resulting with paired and unpaired magnetic configuration, using a) simulation and b) experimental data. The experimental data were analyzed by a magnetic field meter.

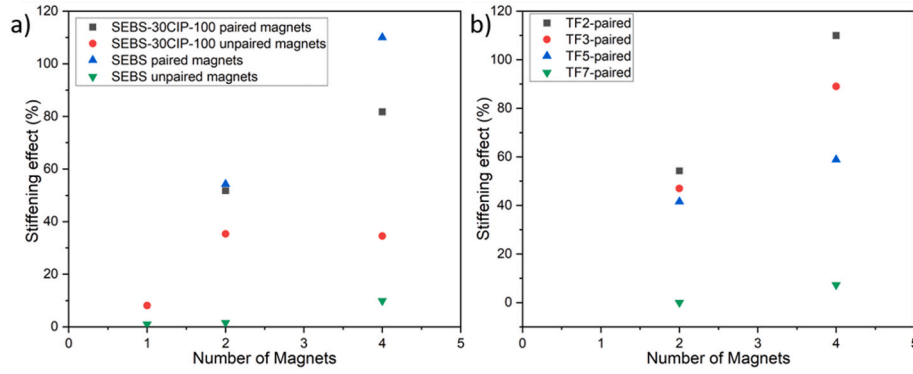


Fig. 5. a) Stiffening effect of SEBS-30CIP-100 and SEBS 3D printed samples and b) SEBS samples with different shore hardness. The samples were printed with 100% infill density and magneto-mechanical behavior was investigated using paired and unpaired magnet configuration with a pre-load of 10 N and deformation of 1%.

effect in SEBS samples using paired and unpaired magnet configurations are shown. Based on the above results, the study was continued with a pre-load of 10 N and 1% deformation. As expected, the paired magnet configuration resulted in an increase in the stiffening effect also for the pure SEBS sample (Fig. 5a). Due to the attraction force between the paired magnets, the SEBS sample was pre-compressed and showed a stiffening effect even without CIP.

Due to the CIP filler, the SEBS-30CIP-100 sample resulted in higher stiffening (*i.e.*, MR effect) due to the high magnetic flux through the sample (Fig. 4). However, similar to the pure SEBS samples, the additional attraction force between the magnets results in a higher pre-compression, which thereby leads to an overestimated MR effect of the sample. It can be expected that the overestimation of the MR effect is lower in this case, due to the higher Shore hardness of the SEBS-30CIP-100. Upon adding CIP to the SEBS matrix, the Shore A hardness increases from 22 to 30, which further leads to a result in an increase in the material stiffness and higher compression modulus [55].

To predict the overestimation of the MR effect (resulting from the additional magnetic attraction force) due to the changing of Shore A hardness, SEBS samples were printed with four different levels of Shore A hardness, namely 22, 30, 48, and 70. As shown in Fig. 5b, it was observed that the softer the matrix, the higher the stiffening effect. It is evident, that for the SEBS-CIP samples also, an overestimation of the MR effect can be expected.

From this observation, we infer that a paired magnetic configuration has an additional effect on the compression test measurements. The additional stiffening effect is due to the magnetic force of attraction in

the paired configuration, which adds up with the mechanical load and thus to a pre-compression since they are unidirectional. A free-body diagram, as shown in Fig. 6, can be used to better explain this phenomenon.

The force equalization for the SEBS and SEBS-30CIP-100 sample in Fig. 6a and b results to:

$$N_{LS} = F_{load} + m_u g + m_s g + F_M \quad (6)$$

The force equalization for SEBS-30CIP-100 in Fig. 6c results to:

$$N_{LS} = F_{load} + m_s g + F_L \quad (7)$$

From Equation (6), it is apparent that an extra force F_M acts on the sample along with the compression loading F_{load} that is applied during the test. This extra force F_M is the magnetic force of attraction between the two paired magnets and acts on both SEBS and SEBS-30CIP-100 resulting in an additional unwanted compression.

In Equation (7), this extra force F_M is absent because of the unpaired magnet configuration. However, a magnetic force of attraction F_L exists. It is worth mentioning that the attraction force F_L also exists for SEBS-30CIP-100 in paired magnet configuration as seen in Fig. 6b. Nevertheless, this force cancels out due to the attraction force F_U which is equal to F_L . In comparison to F_M the attraction force between the paired magnets, F_L in unpaired magnet configuration is much smaller. However, with an increasing number of unpaired magnets, this force increases and thereby, has an effect on the magneto-mechanical compression testing of the MREs. Additionally, it can be hypothesized that the observed deformation in the sample SEBS-30CIP-15, is because

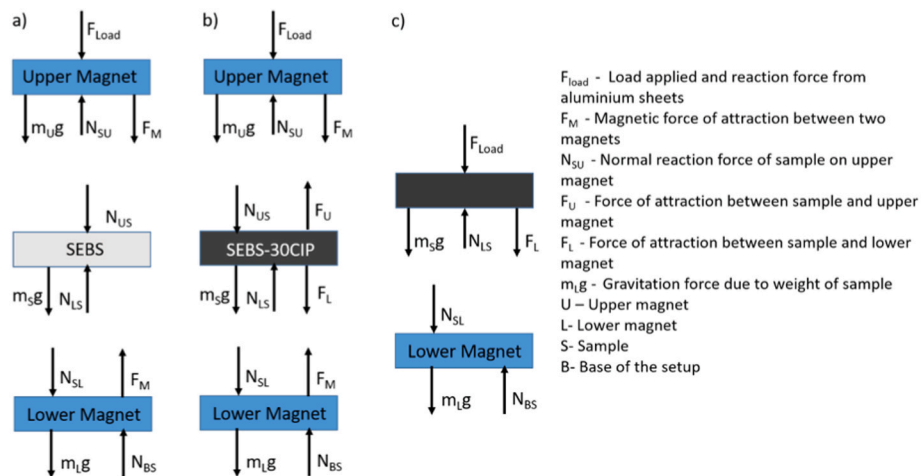


Fig. 6. Free-body diagrams for compression test using a paired magnet configuration with a) SEBS and b) SEBS-30CIP-100; and using an unpaired magnet configuration with c) SEBS-30CIP-100.

of F_L on the sample and the less structural stiffness of the sample.

To experimentally validate our inference from the free-body diagram, simple dimension measurements were performed using a non-metallic digital caliper. The results obtained from these measurements are presented in Table S1. It is observed that the paired magnets pre-compress the sample in between, due to the magnetic force of attraction and this pre-compression is significant. However, the unpaired magnet configuration has almost no pre-compression effect on the sample. Based on the analysis of the magneto-mechanical compression setup unpaired magnet configuration with pre-load of 10 N was used to continue this study.

3.4. Effect of sample height on magnetic flux distribution

Using an unpaired configuration, it can be expected that the magnetic flux measured on top of the sample will be lower in comparison to the bottom surface. Therefore, SEBS-30CIP-100 was printed in three different heights, namely 3, 5 and 7 mm. From FEMM simulation data (Fig. 7a), it was observed that the magnetic flux at the center of the sample cross-section was similar for the three different sample heights. However, as expected, the magnetic flux on top of the sample increased by increasing the external magnetic field. Similar to the previous analysis, the magnetic flux was measured on top of the SEBS-30CIP-100 samples with a magnetic field meter (Fig. 7b). A clear depiction of the change in magnetic flux by varying the height of the sample could be observed. It is notable that the difference in magnetic flux for the different sample heights increases by increasing the magnetic field. Gordaninejad et al. reported a similar observation where they analyzed the magnetic flux for MRE samples of different heights for a given filler particle concentration [42]. They demonstrated that there is no effect of the sample height on the MR effect by assuming that the magnetic flux density decreases by increasing the sample height and therefore plotting the change in modulus versus the magnetic flux density.

The difference between simulated and experimental data can be explained by the magnetic properties in the discretized volume of a cell unit. For the simulated values the magnetic flux is almost similar, whereas for the experimental data the thickness affects the magnetic flux as mentioned previously. The discrepancy cannot be simply explained by the difference in the relative magnetic permeability for the simulated and experimental results (Fig. 4). For the modeling, the magnetic properties in all the cells of discrete volume are constant. In the experiment, the samples are based on a composite consisting of a ferromagnetic filler and a paramagnetic SEBS matrix. The heterogeneous composite will result in a microscopic inhomogeneous magnetic flux density within the sample, which shall decrease with sample thickness.

It is noteworthy, that for the simulation and the experiments the magnetic flux at the center of the sample surface had a minimum value

and the flux increased towards the edge of the samples as shown in Fig. 8. This observation has been made for all the samples with 100% infill and can be explained by the magnetic field lines, which are denser near the sample edge and lowers through the center as shown in the simulation results. The discrepancy between the simulated data and the measured value can be explained by the microscopic inhomogeneous magnetic flux density in the composite as mentioned earlier.

3.5. Magnetorheological behavior of MRE structures with honeycomb infill pattern under compression mode

Based on the analysis of the magneto-mechanical compression setup unpaired magnet configuration with pre-load of 1 N was used to investigate the MRE honeycomb structures. All samples were printed at a height of 5 mm and the MR effect was investigated at a constant magnetic field of 0.357 T (using the same 10 mm thick NdFeB ferromagnet).

The different honeycomb structures were achieved by the variation of the infill density during the 3D printing process. In Fig. 9, optical microscopic pictures of honeycomb structures with different infill densities are demonstrated. To have a better understanding, the values of the cell thickness and the wall size, analyzed from the microscopic pictures, are reported in Table S2.

As indicated in Table S2, the wall thickness is similar between 15, 20, and 25% infill densities and does not vary significantly. Above 30% infill density, the wall thickness increases significantly. As expected, the cell size shows a decreasing trend with an increase in infill density. Understandably, the sample SEBS-30CIP-15 has the highest cell size while the SEBS-30CIP-50 has the lowest. Owing to this reason, the honeycomb structure based on 15% infill density was not stable for MR effect measurements. The geometrical stiffness of the sample was low and deformation was observed during the application of an external magnetic field with an unpaired 10 mm thick NdFeB.

Unfortunately, the magnetic flux could not be reliably measured using our magnetic field meter. Therefore, only simulation was performed on the MRE sample with 20% infill density. A vertical cross-section of the sample SEBS-30CIP-20 was used for the simulation as shown in Fig. 10. The figure shows that the magnetic field lines deviate toward the walls within the MRE structures. Furthermore, it is observed that the magnetic flux density is higher at the rim and the edges of the walls within the sample. Fig. S7 shows the simulated magnetic flux density plot over the sample SEBS-30CIP-20, across its cross-section.

To calculate the MR effect in honeycomb structures, cyclic measurements with a pre-compression were performed and 10 cycles were performed. Fig. 11 demonstrates the cyclic measurements at different compressions (1%, 2%, 4% and 10%). The MATLAB polyfit function was used to find the slope of the best fit line of the loading phase in the 9th cycle, as shown in Fig. 11. It was observed that at a low compression

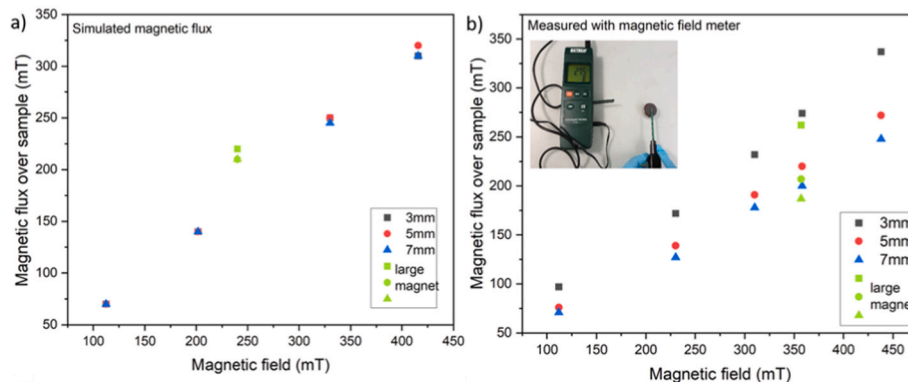


Fig. 7. a) Simulated values for magnetic flux and b) experimental values for magnetic flux for SEBS-30CIP-100 samples with three different heights, namely 3, 5, and 7 mm.

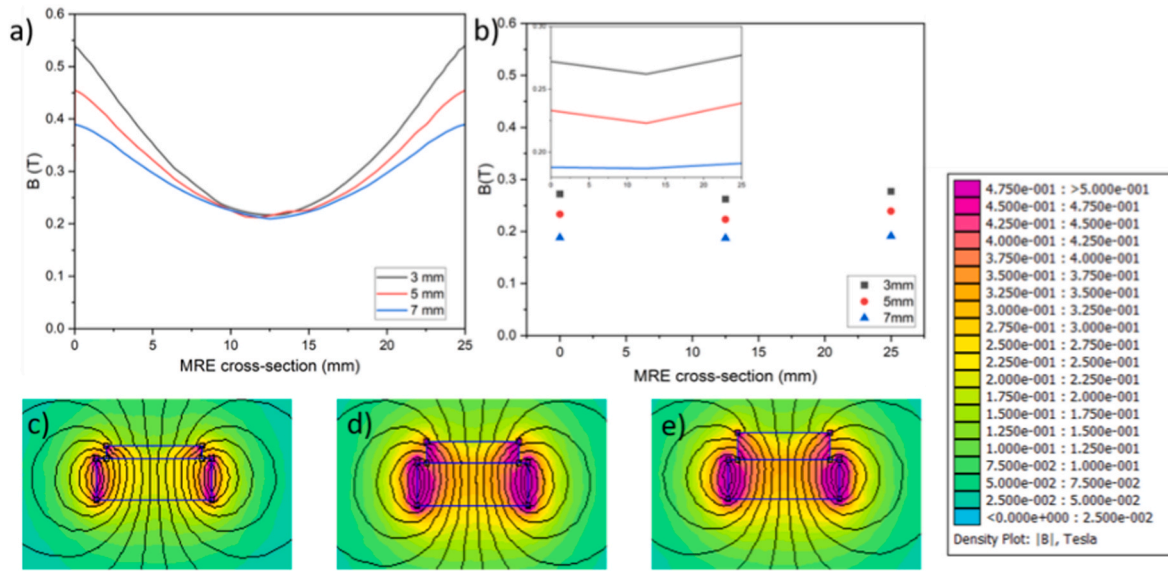


Fig. 8. a) Simulated and b) Experimental magnetic flux measured on top of the SEBS-30CIP-100 sample, across the cross-section. Different sample heights of 3, 5, and 7 mm were used for the simulation and the experimental measurements. Simulation of magnetic field lines in a SEBS-30CIP-100 sample with a height of c) 3 mm, d) 5 mm, and e) 7 mm. A single large NdFeB (10 mm thick) ferromagnet was used to produce the magnetic field in both experiment and simulation.

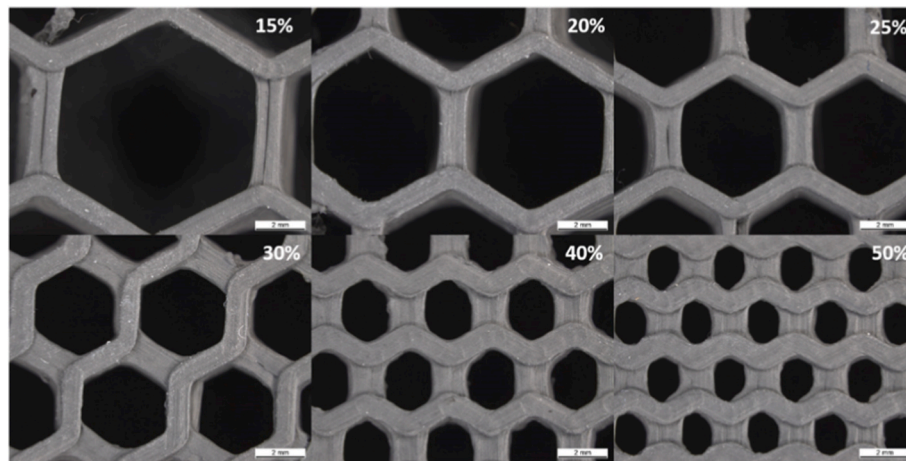


Fig. 9. Optical microscopy analysis of the wall thickness and cell size for the different honeycomb samples achieved by changing the printing infill density from 15 to 50%. All samples have a diameter of 25 mm and a height of 5 mm. A magnification of 11.3x was used for all the images.

level, the loading curve was close to linear. However, at increased compression range, the linearity of the loading curve disappeared. The multiple cyclic tests were performed to minimize the Mullins effect [56, 57].

The Mullins effect describes the stress softening behavior of hyperelastic materials and is a viscoelastic effect [58]. Mullins et al. reported that the stress-strain curve obtained after "conditioning" deformation cycles are more significant and useful than the curve obtained in the first cycle. It has been reported that during cyclic loading-unloading, the stress softening behavior of the elastomer is initially high, while it becomes negligible after 5–10 cycles [59]. Gan et al. studied the effect of magnetic flux density, pre-compression, compression mode and anisotropy of the MRE on magneto-induced Mullins effect in magnetorheological elastomer [60].

To better explain the Mullins effect in our experiments, a drift in force was further analyzed in Fig. S8. The drift in the maximum force and the minimum force during the loading phase of the cycle has been plotted against the number of cycles, for different compression ranges. Due to the stress softening the highest drift occurs between the first and

second cycles and it decreases with an increase in cycle number. A similar observation has been reported by Francesca et al., where carbon black-reinforced rubber was investigated [61].

Comparing the various compression ranges a decrease in MR effect by increasing the compression range could be observed (Fig. 12). This observation is in good agreement with previously reported data for compression testing of MREs fabricated by casting method [40,41]. Both Kallio et al. and Schubert et al. reported in their work that MREs show a higher MR effect in low strain regions. Furthermore, the infill % also has a significant impact on the MR effect. SEBS-30CIP-20/25 samples have a higher MR effect than samples with higher infill%, as shown in Fig. 12b. The maximum relative MR effect obtained with these samples were 128% and 61.3% respectively, which is comparatively higher than other 3D printed MREs in literature. Bastola et al., reported a maximum relative MR effect of 65.2% and 30.1% for their hybrid MRE structures filled with MR fluids and MR elastomers respectively [24]. To confirm if the MR effect is an effect of the geometrical stiffness, a sample with an equivalent effective area as SEBS-30CIP-20 was printed with 100% infill (from here on referred to as SEBS-30CIP-100_2). Both samples showed

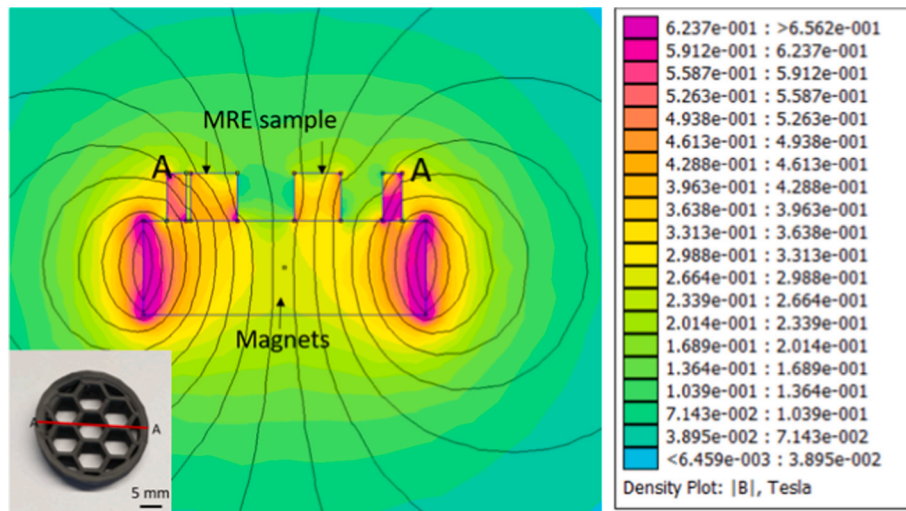


Fig. 10. Simulated magnetic flux lines through an MRE sample with 20% infill density and 5 mm height. The simulation was performed considering the cross-section of the sample as shown using the line A-A. The wall thickness and cell size for the simulation have been measured using an optical microscopy picture (Fig. 9). A 10 mm thick NdFeB magnet has been used for application of the external magnetic field.

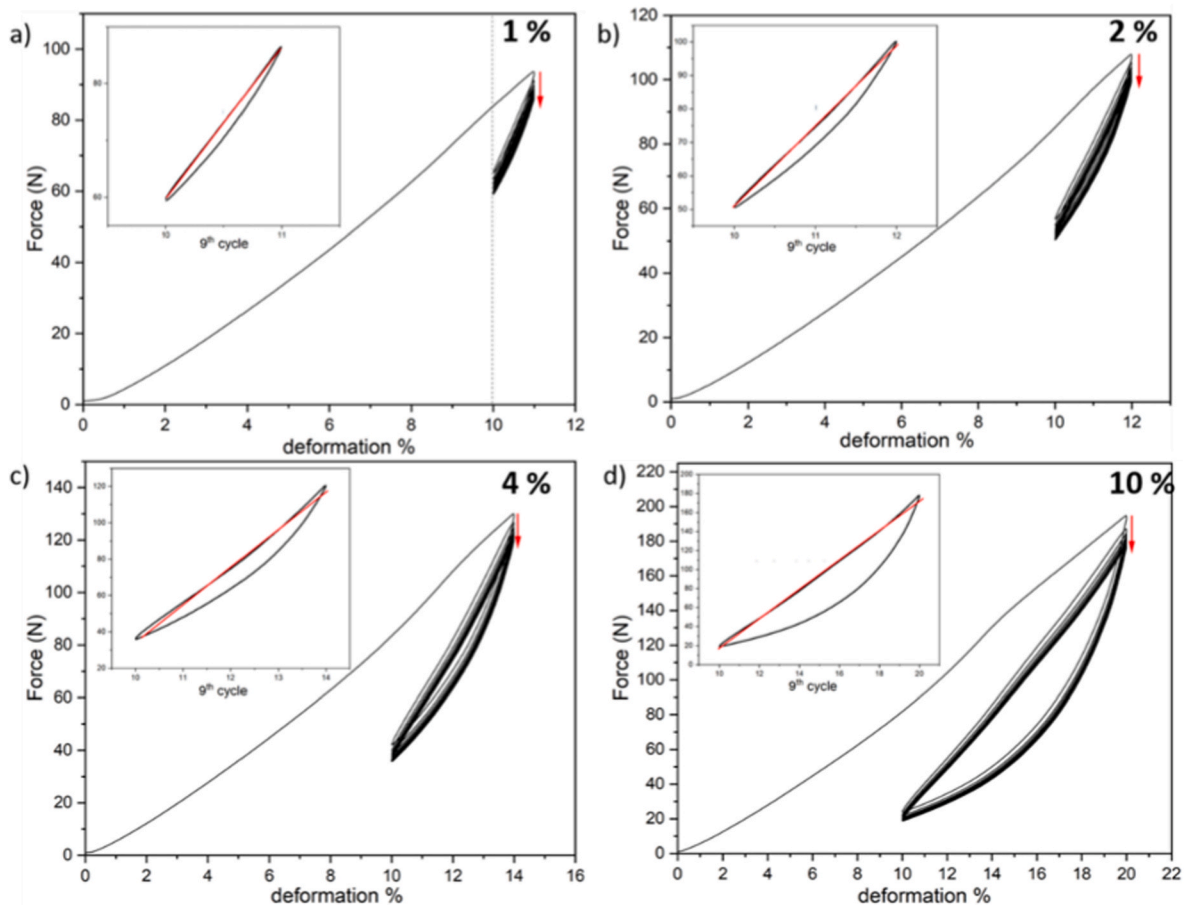


Fig. 11. Cyclic measurements of SEBS-30CIP-100 sample, where a pre-compression of 10% is applied from the second cycle. The measurements were done for various compression range, namely, 1%, 2%, 4% and 10%. Similar experiments were done for SEBS-30CIP sample with varying infill density.

same stiffness under compression loading, without a magnetic field (Fig. S9). However, in presence of a magnetic field, SEBS-30CIP-20 showed a higher MR effect than SEBS-30CIP-100_2. The SEBS-30CIP-100_2 sample showed a comparable MR effect to SEBS-30CIP-100 as shown in Fig. 12. Thereby, it can be confirmed, that

the improved MR effect is not due to geometrical stiffness.

As discussed previously, the magnetic flux density is inhomogeneous within the honeycomb sample. The magnetic field lines are more concentrated at the rim and the edges of the walls inside (Fig. 10). Thereby, the way the magnetic field lines are distributed within the

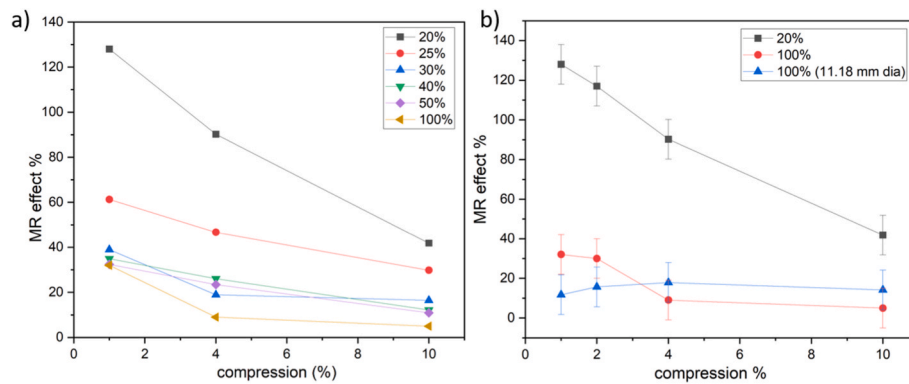


Fig. 12. MR effect measured using the slope from the 9th cycle of the cyclic compression test with 10% pre-compression and 10 mm thick NdFeB magnet, a) for samples with various honeycomb-patterned in-fill densities, b) for samples with 20% infill and samples with 100% infill (25 mm and 11.18 mm diameter). The compression range varied from 1 to 10%. All samples used are 5 mm in height.

sample will result in a higher MR effect. It is observed in Fig. 12a, that samples with 30, 40, and 50% infill have approximately similar MR effect values as the 100% infill sample. The similarity in MR effect could be an effect of the larger wall thickness of those samples (Table S2) which result in a similar magnetic flux density profile as in the case of SEBS-30CIP-100.

In literature different works have also reported the absolute MR effect in order to evaluate the magnetorheological properties of MREs [62, 63]. The absolute MR effect for all SEBS-30CIP samples with varying infill density is shown in Table S3. The highest absolute MR effect could be observed for the 20% infill sample (SEBS-30CIP-20). The samples with 25% infill and 100% infill show a similar absolute MR effect value. However, it is worthwhile to mention that the samples with 25% infill have a significantly lower stiffness in comparison to the 100% sample. For samples with 30, 40 and 50% infill density, the absolute MR effect was the lowest and was lower in comparison to the SEBS-30CIP-100 at all deformation ranges. Unfortunately, for 3D-printed hybrid MREs, the absolute MR effect has not been reported so far and therefore a comparison of our results with the literature cannot be drawn.

4. Conclusion

To investigate the lightweight structure concept for MREs, soft honeycomb-patterned magnetorheological structures based on TPE matrix and CIP filler particles were successfully printed with FDM technology. A study of the compression testing setup and the various testing parameters like pre-load, pre-strain, paired, and unpaired magnet configuration allowed for a comparison between the samples with different infills while identifying artifacts from test configurations. The study showed that a paired magnet configuration leads to an over-estimated MR effect. To explain the overestimation, a free-body diagram made apparent that there is an additional magnetic force of attraction between the magnets in the paired configuration. The hyperelastic materials showed a non-linear force strain curve and a pre-compression resulted in a shift of the strain range and therefore a change in slope in the force-strain curve. Cycling tests were performed to eliminate the stress softening behavior due to the Mullin's effect. Finally, it was observed that samples with less infill density showed a higher MR effect. The increase is not caused by the lowered geometrical stiffness. Using FEM analysis indicated that the effect is caused by the introduced inhomogeneous magnetic field inside the honeycomb pattern infill.

We conclude that the MR effect in MREs can not only be tuned by changing the filler content or the matrix material to a different Young's modulus, but also by using a lightweight, cellular structure concept.

We only focused on honeycomb structure infill for this study, other infill patterns should be investigated in the future. Additive manufacturing such as multi-material FDM printing will make it feasible

in future to tune the MR effect and produce complex "soft" cellular structures with even higher MR effect.

Credits

Somashree Mondal- Conceptualization, Methodology, Investigation, Validation, Writing- Original Draft, Visualization, **Robert Katzschmann**- Validation, Writing- Reviewing and Editing, Supervision, **Frank Clemens**- Conceptualization, Validation, Writing- Reviewing and Editing, Supervision, Funding acquisition.

Declaration of competing interest

The authors declare that they have no known competing financial interests or personal relationships that could have appeared to influence the work reported in this paper.

Data availability

Data will be made available on request.

Acknowledgment

This project has received funding from the SMART project, European Union's Horizon 2020 research and innovation under the Marie Skłodowska-Curie (grant agreement ID 860108).

The authors would like to also thank Arturo Tagliabue for his help with the FEMM simulation and Dr. Arun Ichangi for his help with the SEM measurements.

Appendix A. Supplementary data

Supplementary data to this article can be found online at <https://doi.org/10.1016/j.compositesb.2023.110498>.

References

- [1] Carlson JD, Jolly MR. MR fluid, foam and elastomer devices. *Mechatronics* Jun. 2000;10(4):555–69. [https://doi.org/10.1016/S0957-4158\(99\)00064-1](https://doi.org/10.1016/S0957-4158(99)00064-1).
- [2] Kaleta J, Królewicz M, Lewandowski D. Magnetomechanical properties of anisotropic and isotropic magnetorheological composites with thermoplastic elastomer matrices. *Smart Mater Struct* Jul. 2011;20(8):085006. <https://doi.org/10.1088/0964-1726/20/8/085006>.
- [3] Burgaz E, Goksuzoglu M. Effects of magnetic particles and carbon black on structure and properties of magnetorheological elastomers. *Polym Test* Jan. 2020; 81:106233. <https://doi.org/10.1016/j.polymertesting.2019.106233>.
- [4] Tagliabue A, Eblagon F, Clemens F. Analysis of styrene-butadiene based thermoplastic magnetorheological elastomers with surface-treated iron particles. *Polymers* Jan. 2021;13(10). <https://doi.org/10.3390/polym13101597>. Art. no. 10.
- [5] Vatandoost H, Hemmatian M, Sedaghati R, Rakheja S. Dynamic characterization of isotropic and anisotropic magnetorheological elastomers in the oscillatory squeeze

- mode superimposed on large static pre-strain. *Compos B Eng* Feb. 2020;182: 107648. <https://doi.org/10.1016/j.compositesb.2019.107648>.
- [6] Bastola AK, Hossain M. A review on magneto-mechanical characterizations of magnetorheological elastomers. *Compos B Eng* Nov. 2020;200:108348. <https://doi.org/10.1016/j.compositesb.2020.108348>.
 - [7] Ginder JM, Nichols ME, Elie LD, Tardiff JL. Magnetorheological elastomers: properties and applications. In: *Smart structures and materials* 1999. vol. 3675. Smart Materials Technologies; Jul. 1999. p. 131–8. <https://doi.org/10.1117/12.352787>.
 - [8] Lokander M, Reitberger T, Stenberg B. Oxidation of natural rubber-based magnetorheological elastomers. *Polym Degrad Stab* Dec. 2004;86(3):467–71. <https://doi.org/10.1016/j.polymdegradstab.2004.05.019>.
 - [9] Chen L, Gong X, Li W. Damping of magnetorheological elastomers. *Chin J Chem Phys* Dec. 2008;21(6):581–5. <https://doi.org/10.1088/1674-0068/21/06/581-585>.
 - [10] Jolly MR, Carlson JD, Muñoz BC. A model of the behaviour of magnetorheological materials. *Smart Mater Struct* Oct. 1996;5(5):607–14. <https://doi.org/10.1088/0964-1726/5/5/009>.
 - [11] Böse H. Viscoelastic properties of silicone-based magnetorheological elastomers. *Int J Mod Phys B* Nov. 2007;21(28n29):4790–7. <https://doi.org/10.1142/S0217979207045670>.
 - [12] Li R, Sun LZ. Viscoelastic responses of silicone-rubber-based magnetorheological elastomers under compressive and shear loadings. *J Eng Mater Technol* März 2013; 135(2). <https://doi.org/10.1115/1.4023839>.
 - [13] Wei B, Gong X, Jiang W. Influence of polyurethane properties on mechanical performances of magnetorheological elastomers. *J Appl Polym Sci* 2010;116(2): 771–8. <https://doi.org/10.1002/app.31474>.
 - [14] Zhao D, Zhao Z, Dai X, Wang S, Liu S, Liu Y. Study on mechanical properties of a novel polyurethane sponge magnetorheological elastomers in compressive mode. *Mater Res Express* Sep. 2019;6(11):116101. <https://doi.org/10.1088/2053-1591/ab439f>.
 - [15] Zajac P, Lewandowski D, Gasperowicz A. Isotropic magnetorheological elastomers with thermoplastic matrices: structure, damping properties and testing. *Smart Mater Struct* 2010;19:045014. <https://doi.org/10.1088/0964-1726/19/4/045014>.
 - [16] Ren L, et al. 3D magnetic printing of bio-inspired composites with tunable mechanical properties. *J Mater Sci* Oct. 2018;53(20):14274–86. <https://doi.org/10.1007/s10853-018-2447-5>.
 - [17] Li X, et al. Limpet tooth-inspired painless microneedles fabricated by magnetic field-assisted 3D printing. *Adv Funct Mater* 2021;31(5):2003725. <https://doi.org/10.1002/adfm.202003725>.
 - [18] Bollig LM, Hilpisch PJ, Mowry GS, Nelson-Cheeseman BB. 3D printed magnetic polymer composite transformers. *J Magn Magn Mater* Nov. 2017;442:97–101. <https://doi.org/10.1016/j.jmmm.2017.06.070>.
 - [19] Kobayashi K, Ikuta K. 3D magnetic microactuator made of newly developed magnetically modified photocurable polymer and application to swimming micromachine and microscrowpump. In: 2009 IEEE 22nd international conference on micro electro mechanical systems; Jan. 2009. p. 11–4. <https://doi.org/10.1109/MEMSYS.2009.4805306>.
 - [20] Kim Y, Yuk H, Zhao R, Chester SA, Zhao X. Printing ferromagnetic domains for untethered fast-transforming soft materials. *Nature* Jun. 2018;558(7709). <https://doi.org/10.1038/s41586-018-0185-0>. Art. no. 7709.
 - [21] Roh S, et al. Magnetic actuators: 3D-printed silicone soft architectures with programmed magneto-capillary reconfiguration. *Adv Mater Technol* 2019;4(4): 1970021. <https://doi.org/10.1002/admt.201970021>.
 - [22] Joyee EB, Pan Y. A fully three-dimensional printed inchworm-inspired soft robot with magnetic actuation. *Soft Robot* Jun. 2019;6(3):333–45. <https://doi.org/10.1089/soro.2018.0082>.
 - [23] Bastola AK, Hoang VT, Li L. A novel hybrid magnetorheological elastomer developed by 3D printing. *Mater Des* Jan. 2017;114:391–7. <https://doi.org/10.1016/j.matdes.2016.11.006>.
 - [24] Bastola AK, Paudel M, Li L. Development of hybrid magnetorheological elastomers by 3D printing. *Polymer* Aug. 2018;149:213–28. <https://doi.org/10.1016/j.polymer.2018.06.076>.
 - [25] Bastola A, Paudel M, Li L. Line-patterned hybrid magnetorheological elastomer developed by 3D printing. *J Intell Mater Syst Struct* Feb. 2020;31(3):377–88. <https://doi.org/10.1177/1045389X19891557>.
 - [26] Krueger H, Vaezi M, Yang S. 3D printing of magnetorheological elastomers (MREs) smart materials. *Mai* 2014. p. 213–8. <https://doi.org/10.3850/978-981-09-0446-3.088>.
 - [27] Ji Z, Yan C, Yu B, Wang X, Zhou F. Multimaterials 3D printing for free assembly manufacturing of magnetic driving soft actuator. *Adv Mater Interfac* 2017;4(22): 1700629. <https://doi.org/10.1002/admi.201700629>.
 - [28] Lantean S, et al. 3D printing of magnetoresponsive polymeric materials with tunable mechanical and magnetic properties by digital light processing. *Adv Mater Technol* 2019;4(11):1900505. <https://doi.org/10.1002/admt.201900505>.
 - [29] 14:00-17:00, "ISO/ASTM 52900:2021," ISO. <https://www.iso.org/cms/render/live/en/sites/isoorg/contents/data/standard/07/45/74514.html> (accessed Mar. 31, 2022).
 - [30] Khatir B, Lappe K, Noetzel D, Pursche K, Hanemann T. A 3D-printable polymer-metal soft-magnetic functional composite—development and characterization. *Materials* Feb. 2018;11(2). <https://doi.org/10.3390/ma11020189>. Art. no. 2.
 - [31] Ralchev M, Mateev V, Marinova I. Magnetic properties of FFF/FDM 3D printed magnetic material," in *2021 17th Conference on electrical machines, Drives and power systems. ELMA*; Jul. 2021. p. 1–5. <https://doi.org/10.1109/ELMA52514.2021.9503037>.
 - [32] Rajkumar S. Strength and stiffness characteristics of A3003 aluminum honeycomb core sandwich panels. *Mater Today Proc* Jan. 2021;37:1140–5. <https://doi.org/10.1016/j.matpr.2020.06.348>.
 - [33] Andrew JJ, Ubaid J, Hafeez F, Schiffer A, Kumar S. Impact performance enhancement of honeycombs through additive manufacturing-enabled geometrical tailoring. *Int J Impact Eng* Dec. 2019;134:103360. <https://doi.org/10.1016/j.ijimpeng.2019.103360>.
 - [34] Alia R, Al-Ali O, Kumar S, Cantwell W. The energy-absorbing characteristics of carbon fiber-reinforced epoxy honeycomb structures. *J Compos Mater* 2019;53(9): 1145–1157. Apr. <https://doi.org/10.1177/0021998318796161>.
 - [35] Sun G, Chen D, Wang H, Hazell PJ, Li Q. High-velocity impact behaviour of aluminium honeycomb sandwich panels with different structural configurations. *Int J Impact Eng* Dec. 2018;122:119–36. <https://doi.org/10.1016/j.ijimpeng.2018.08.007>.
 - [36] Li T, Wang L. Bending behavior of sandwich composite structures with tunable 3D-printed core materials. *Compos Struct* Sep. 2017;175:46–57. <https://doi.org/10.1016/j.compstruct.2017.05.001>.
 - [37] Chen Y, Li T, Jia Z, Scarpa F, Yao C-W, Wang L. 3D printed hierarchical honeycombs with shape integrity under large compressive deformations. *Mater Des* Jan. 2018;137:226–34. <https://doi.org/10.1016/j.matdes.2017.10.028>.
 - [38] Boczkowska A, Awietjan SF, Pietrzko S, Kurzydowski KJ. Mechanical properties of magnetorheological elastomers under shear deformation. *Compos B Eng* Mar. 2012;43(2):636–40. <https://doi.org/10.1016/j.compositesb.2011.08.026>.
 - [39] Johari MAF, et al. Microstructural behavior of magnetorheological elastomer undergoing durability evaluation by stress relaxation. *Sci Rep* May 2021;11(1). <https://doi.org/10.1038/s41598-021-90484-0>. Art. no. 1.
 - [40] Schubert G, Harrison P. Large-strain behaviour of Magneto-Rheological Elastomers tested under uniaxial compression and tension, and pure shear deformations. *Polym Test* Apr. 2015;42:122–34. <https://doi.org/10.1016/j.polymertesting.2015.01.008>.
 - [41] Kallio M, Lindroos T, Aalto S, Järvinen E, Kärnä T, Meinander T. Dynamic compression testing of a tunable spring element consisting of a magnetorheological elastomer. *Smart Mater Struct* Mar. 2007;16(2):506. <https://doi.org/10.1088/0964-1726/16/2/032>.
 - [42] Gordaninejad F, Wang X, Mysore P. Behavior of thick magnetorheological elastomers. *J Intell Mater Syst Struct* Jun. 2012;23(9):1033–9. <https://doi.org/10.1177/1045389X12448286>.
 - [43] Soria-Hernández CG, Palacios-Pineda LM, Elías-Zúñiga A, Perales-Martínez IA, Martínez-Romero O. Investigation of the effect of carbonyl iron micro-particles on the mechanical and rheological properties of isotropic and anisotropic MREs: constitutive magneto-mechanical material model. *Polymers* Oct. 2019;11(10). <https://doi.org/10.3390/polym11101705>. Art. no. 10.
 - [44] Vatandoost H, Sedaghati R, Rakheja S, Hemmatian M. Effect of pre-strain on compression mode properties of magnetorheological elastomers. *Polym Test* Jan. 2021;93:106888. <https://doi.org/10.1016/j.polymertesting.2020.106888>.
 - [45] Vatandoost H, Hemmatian M, Sedaghati R, Rakheja S. Effect of shape factor on compression mode dynamic properties of magnetorheological elastomers. *J Intell Mater Syst Struct* Sep. 2021;32(15):1678–99. <https://doi.org/10.1177/1045389X20983921>.
 - [46] Boczkowska A, Awietjan SF, Wroblewski R. Microstructure-property relationships of urethane magnetorheological elastomers. *Smart Mater Struct* Sep. 2007;16(5): 1924. <https://doi.org/10.1088/0964-1726/16/5/049>.
 - [47] Vatandoost H, Rakheja S, Sedaghati R. Effects of iron particles' volume fraction on compression mode properties of magnetorheological elastomers. *J Magn Magn Mater* Mar. 2021;522:167552. <https://doi.org/10.1016/j.jmmm.2020.167552>.
 - [48] Koo JH, Khan F, Jang DD, Jung HJ. Dynamic characterization and modeling of magneto-rheological elastomers under compressive loadings. *J Phys Conf Ser* Feb. 2009;149:012093. <https://doi.org/10.1088/1742-6596/149/1/012093>.
 - [49] Wan Y, Xiong Y, Zhang S. Temperature effect on viscoelastic properties of anisotropic magnetorheological elastomers under compression. *Smart Mater Struct* Nov. 2018;28(1):015005. <https://doi.org/10.1088/1361-665X/aaef8>.
 - [50] Farshad M, Benine A. Magnetoactive elastomer composites. *Polym Test* Mai 2004; 23(3):347–53. [https://doi.org/10.1016/S0142-9418\(03\)00103-X](https://doi.org/10.1016/S0142-9418(03)00103-X).
 - [51] Mistik SI, Shah T, Hadimani RL, Siores E. Compression and thermal conductivity characteristics of magnetorheological fluid-spacer fabric smart structures. *J Intell Mater Syst Struct* 2012;23(11):1277–1283, Jul. <https://doi.org/10.1177/1045389X12447295>.
 - [52] Martins A, Fereidooni A, Suleman A, Wickramasinghe V. Test rig development and characterization of magnetorheological elastomers. *Jan. 2017. https://doi.org/10.2514/6.2017-0733*.
 - [53] Brancati R, Di Massa G, Pagano S. Investigation on the mechanical properties of MRE compounds. *Machines* Jun. 2019;7(2). <https://doi.org/10.3390/machines7020036>. Art. no. 2.
 - [54] Tao R. Electro-rheological fluids and magneto-rheological suspensions: proceedings of the 12th international conference. Philadelphia, USA: World Scientific; 2011. p. 16–20. August 2010.
 - [55] Farshad M, Clemens F, Le Roux M. Magnetoactive polymer composite fibers and fabrics—processing and mechanical characterization. *J Thermoplast Compos Mater* Jan. 2007;20(1):65–74. <https://doi.org/10.1177/0892705707070442>.
 - [56] Mullins L. Effect of stretching on the properties of rubber. *Rubber Chem Technol* Jun. 1948;21(2):281–300. <https://doi.org/10.5254/1.3546914>.
 - [57] Mullins L, Tobin N. Theoretical model for the elastic behavior of filler-reinforced vulcanized rubbers. 1957. <https://doi.org/10.5254/1.3542705>.
 - [58] Mullins L. Softening of rubber by deformation. *Rubber Chem Technol* Mar. 1969; 42(1):339–62. <https://doi.org/10.5254/1.3539210>.

- [59] Cantournet S, Desmorat R, Besson J. Mullins effect and cyclic stress softening of filled elastomers by internal sliding and friction thermodynamics model. *Int J Solid Struct* Jun. 2009;46(11):2255–64. <https://doi.org/10.1016/j.ijsolstr.2008.12.025>.
- [60] Gan R, et al. Magneto-induced Mullins effect of anisotropic MREs under compression mode. *Smart Mater Struct* Jan. 2021;30(2):024003. <https://doi.org/10.1088/1361-665X/abd839>.
- [61] Carleo F, Barbieri E, Whear R, Busfield JJC. Limitations of viscoelastic constitutive models for carbon-black reinforced rubber in medium dynamic strains and medium strain rates. *Polymers Sep.* 2018;10(9). <https://doi.org/10.3390/polym10090988>. Art. no. 9.
- [62] Alkhalaf A, Hooshair A, Dargahi J. Composite magnetorheological elastomers for tactile displays: enhanced MR-effect through bi-layer composition. *Compos B Eng Jun.* 2020;190:107888. <https://doi.org/10.1016/j.compositesb.2020.107888>.
- [63] Dong X, Ma N, Qi M, Li J, Chen R, Ou J. The pressure-dependent MR effect of magnetorheological elastomers. *Smart Mater Struct Jun.* 2012;21(7):075014. <https://doi.org/10.1088/0964-1726/21/7/075014>.